Numerical Evaluation of Singular and Near-Singular Potential Integrals

Michael A. Khayat, *Member, IEEE,* and Donald R. Wilton, *Fellow, IEEE*

***Abstract*—A simple and efficient numerical procedure using a singularity cancellation scheme is presented for evaluating singular and near-singular potential integrals with $1/R$ singularities. The procedure not only has several advantages over singularity subtraction methods, but also improves on some aspects of other singularity cancellation methods such as polar and Duffy transformations. A theoretical analysis is presented for triangles, quadrilaterals, tetrahedrons, bricks, and prisms, and numerical results are presented for triangles and prisms.**

I. INTRODUCTION

POTENTIAL integrals involved in the integral equations of electromagnetics are often singular, and therefore require special numerical considerations for their evaluation. Unbounded (but integrable) singularities occur, for example, in the kernels of so-called self-terms in the method of moments where testing and source subdomains coincide. Often quadrature rules for direct treatments of these singularities do not exist. In such situations, *singularity subtraction* or *singularity cancellation methods* are often used.

In the singularity subtraction approach, terms having the same asymptotic behavior as the integrand at the singularity are first subtracted from the integrand, leaving a bounded difference integrand that may be integrated numerically. The subtracted singular term is then analytically integrated and the result added back to the numerically integrated terms to complete the potential evaluation. For a Green's function $G(\mathbf{r},\mathbf{r}')$ with asymptotic behavior $G(\mathbf{r},\mathbf{r}') \underset{\mathbf{r}\to\mathbf{r}'}{\longrightarrow} G^{\mathrm{asym}}(\mathbf{r},\mathbf{r}')$ on a domain $\mathcal{D}$ containing $\mathbf{r}$, the procedure may be summarized as

$$\int_{\mathcal{D}} \mathbf{\Lambda}(\mathbf{r}')G(\mathbf{r},\mathbf{r}')d\mathcal{D}' = \underbrace{\int_{\mathcal{D}} \mathbf{\Lambda}(\mathbf{r}')[G(\mathbf{r},\mathbf{r}') - G^{\mathrm{asym}}(\mathbf{r},\mathbf{r}')]d\mathcal{D}'}_{\text{Integrated numerically}} + \underbrace{\int_{\mathcal{D}} \mathbf{\Lambda}(\mathbf{r}')G^{\mathrm{asym}}(\mathbf{r},\mathbf{r}')d\mathcal{D}'}_{\text{Integrated analytically}} \quad (1)$$

where $\mathbf{\Lambda}(\mathbf{r})$ is a vector (or scalar) basis function.

The singularity subtraction approach relies on the existence of analytically evaluated potential integrals, usually of static form. Many of these have been worked out for various tubular, polygonal, and polyhedral elements for both constant and linearly varying source distributions [1]–[9]. Potentials resulting from even higher order polynomial source variations are also available [6], [10].

Despite its widespread usage, however, the singularity subtraction method has a number of disadvantages, among which are the following.

1) The difference integrand $G(\mathbf{r},\mathbf{r}') - G^{\mathrm{asym}}(\mathbf{r},\mathbf{r}')$, while bounded, generally remains singular in a technical sense because it contains higher order derivatives that are unbounded. In a practical sense, this means the integrand cannot be well approximated by a polynomial in the neighborhood of the singularity, thus limiting the achievable accuracy of Gaussian quadrature rules designed to exactly integrate such polynomials. This fundamentally limits the accuracy achievable by singularity subtraction methods.
2) The singular term(s) $G^{\mathrm{asym}}(\mathbf{r},\mathbf{r}')$ subtracted are usually determined by expanding the integrand in a Taylor series about the singular point, a process that increases in complexity for higher order or singular bases, curvilinear elements [11], or complicated Green's functions where the singularity may appear either in spectral or spatial representations.
3) The complexity of analytical expressions for the integrals of $\Lambda(\mathbf{r}')G^{\mathrm{asym}}(\mathbf{r},\mathbf{r}')$ increases with the complexity of the bases, geometry, and Green's functions involved. Although exact in principle, such terms result from differences between indefinite integrals evaluated at upper and lower integration limits, and the potential for errors resulting from small differences between large numbers often increases dramatically with increased integrand complexity. Furthermore, many of the terms that arise need special treatment for limiting situations such as nearly degenerate geometries or observation points that lie close to subdomain boundaries. Since these numerically difficult cases require a relatively large investment in analytical and programming effort, the subtraction method frequently becomes a costly approach that achieves only modest accuracy in the evaluation of moment matrix contributions.
4) The subtraction method severely disrupts object-oriented paradigms because the source subdomain geometry, basis function, and asymptotic form of the Green's function are inextricably linked in the analytically evaluated self-term integral. A typical contribution to the system moment matrix element requires the computation of an element-to-element interaction matrix of the form

$$\left\langle \mathbf{\Lambda}_i^e; G, \mathbf{\Lambda}_j^f \right\rangle \equiv \int_{\mathcal{D}^e}\int_{\mathcal{D}^f} \mathbf{\Lambda}_i^e(\mathbf{r}) \cdot \mathbf{\Lambda}_j^f(\mathbf{r}')G(\mathbf{r},\mathbf{r}')d\mathcal{D}'d\mathcal{D} \quad (2)$$

Manuscript received October 19, 2004; revised February 23, 2005.

The authors are with the Department of Electrical and Computer Engineering, University of Houston, Houston, TX 77204-4793 USA (e-mail: jandhyala@ee.washington.edu).

Digital Object Identifier 10.1109/TAP.2005.856342

corresponding to the interaction between the jth basis function on element f and the ith testing function on element e ($\mathbf{\Lambda}_j^f(\mathbf{r})$ and $\mathbf{\Lambda}_i^e(\mathbf{r})$, respectively), and a Green's function kernel. A general-purpose object-oriented code such as EIGER [12] computes the element matrix object $\left[\left\langle \mathbf{\Lambda}_i^e; G, \mathbf{\Lambda}_j^f \right\rangle\right]$ by calling procedures and exchanging data with other objects, namely, the source and test basis functions, subdomain element geometries, quadrature rules, and Green's functions. In a well-designed code, such objects should be as independent as possible so that the element matrix object can be constructed by independent calls with data exchanges to these secondary objects.

Clearly, despite its workhorse status, the singularity subtraction method has major disadvantages. To extend the capabilities, accuracy, and maintainability of general-purpose codes, the subtraction method is being replaced in favor of the purely numerical quadrature schemes reported here. These schemes employ singularity cancellation methods in which a change of variables is chosen such that the Jacobian of the transformation cancels the singularity. In contrast to the singularity subtraction method, the resulting integrand is analytic in the transformed variables on the element geometry, and hence is amenable to integration by a Cartesian product of Gauss–Legendre rules. The scheme may be made transparent to the user by transforming the sample points and weights back to the original parametric domain, resulting in a purely numerical scheme for integrating singular and near-singular kernels.

An example of the singularity cancellation approach is the method popularly known as the Duffy method [13]–[15]. The Duffy method, however, has two drawbacks.

1) It produces an angular variation about the singular point in the resulting integrand.
2) It appears not to work well when applied to *nearly singular* integrals occurring when an observation point is *near* a source point.

In this paper, we present a purely numerical singularity cancellation method that not only removes the angular dependence about the singular point but also is effective in computing nearly singular integrals [16]–[18]. The discussion is divided into two sections dealing with 2-D and 3-D geometries.

II. 2-D GEOMETRY—TRIANGLES AND QUADRILATERALS

A. Theory

To evaluate potential integrals of the form

$$\mathbf{I} = \int_{\mathcal{D}} \mathbf{\Lambda}(\mathbf{r}') \frac{e^{-jkR}}{4\pi R} d\mathcal{D} \tag{3}$$

on triangular domains $\mathcal{D}$, consider the projection of a nearby observation point $\mathbf{r}$ onto a triangular element with vertices at $\mathbf{r}_1$, $\mathbf{r}_2$, $\mathbf{r}_3$. From the projection point $\mathbf{r}_0$, we subdivide the triangle into three subtriangles, as shown in Fig. 1, and evaluate the partial potential contribution from each. The analysis is detailed for subtriangle 1, shown in Fig. 2. The figure shows a local xyz coordinate system with origin at the projection point, corresponding to *local* vertex 1. We also use local coordinates and geometrical quantities in the subtriangle defined as

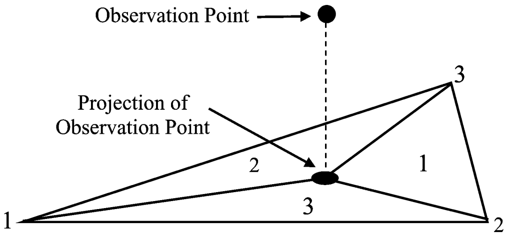

Fig. 1. Subdividing a triangle into subtriangles about the projected observation point.

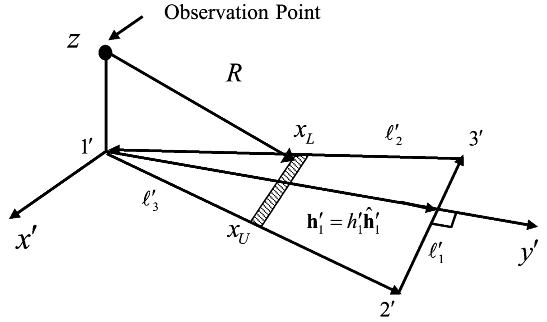

Fig. 2. Subtriangle coordinate system and geometry of subtriangle 1.

$$\begin{aligned}
\mathbf{r}_1' &= \mathbf{r}_0, & \boldsymbol{\ell}_1' &= \mathbf{r}_3' - \mathbf{r}_2' \\
\mathbf{r}_2' &= \mathbf{r}_2 \to \mathbf{r}_3 \to \mathbf{r}_1, & \boldsymbol{\ell}_2' &= \mathbf{r}_1' - \mathbf{r}_3' \\
\mathbf{r}_3' &= \mathbf{r}_3 \to \mathbf{r}_1 \to \mathbf{r}_2, & \boldsymbol{\ell}_3' &= \mathbf{r}_2' - \mathbf{r}_1' \\
\hat{\mathbf{n}}' &= \frac{\boldsymbol{\ell}_1' \times \boldsymbol{\ell}_2'}{\left|\boldsymbol{\ell}_1' \times \boldsymbol{\ell}_2'\right|}, & A' &= \frac{\hat{\mathbf{n}}' \cdot \boldsymbol{\ell}' \times \boldsymbol{\ell}_2'}{2} \\
\mathbf{h}_1' &= \frac{2A'}{\left|\boldsymbol{\ell}_1'\right|^2} \boldsymbol{\ell}_1' \times \hat{\mathbf{n}}'
\end{aligned} \tag{4}$$

where the arrows indicate permutations on the right-hand side of the equalities needed to go from treating subtriangle 1 to subtriangles 2 and 3 of Fig. 1. Note that primes are used to indicate geometrical quantities on a subtriangle.

The integral over subtriangle 1 has the form

$$\mathbf{I}_1 = \int_0^{h_1'} \int_{x_L(y')}^{x_U(y')} \mathbf{\Lambda}(\mathbf{r}') \frac{e^{-jkR}}{4\pi R} dx' dy' \tag{5}$$

where $\mathbf{\Lambda}(\mathbf{r}')$ is a vector or scalar basis function, $R = \sqrt{(x')^2 + (y')^2 + z^2}$ is the distance between source and observation points, and $e^{-jkR}/(4\pi R)$ is the 3-D Green's function. The integration limits on the inner integral are

$$x_L = \hat{\mathbf{n}}' \cdot \left(\hat{\mathbf{h}}_1' \times \boldsymbol{\ell}_2'\right)(1 - \xi_1') \tag{6}$$

and

$$x_U = -\hat{\mathbf{n}}' \cdot \left(\hat{\mathbf{h}}_1' \times \boldsymbol{\ell}_3'\right)(1 - \xi_1'). \tag{7}$$

The normalized area (simplex) coordinate [19] ξ_1' is unity at $y'=0$ and zero at $y'=h_1'$, i.e., $y'=h_1'(1-\xi_1')$. To eliminate singularities or near-singularities associated with the $1/R$ term, we let

$$du = \frac{dx'}{R} = \frac{dx'}{\sqrt{(x')^2+(y')^2+z^2}} \tag{8}$$

yielding

$$u(x') = \sinh^{-1}\frac{x'}{\sqrt{(y')^2+z^2}} = \frac{1}{2}\ln\left(\frac{R+x'}{R-x'}\right). \tag{9}$$

Equation (5) now becomes

$$\begin{aligned}\mathbf{I}_1 &= \frac{1}{4\pi}\int_0^{h_1'}\int_{u_L}^{u_U}\boldsymbol{\Lambda}(\mathbf{r}')e^{-jkR}du\,dy' \\ &\approx \frac{1}{4\pi}\sum_{i=1}^{K}\sum_{j=1}^{M} w_i^{\mathrm{GL}}w_j^{\mathrm{GL}}h_1'\left(u_U^{(j)}-u_L^{(j)}\right) \\ &\quad\times\boldsymbol{\Lambda}(\mathbf{r}'^{(i,j)})e^{-jkR^{(i,j)}}\end{aligned} \tag{10}$$

where $R=\sqrt{(y')^2+z^2}\cosh u$ so that the integrand is analytic in u and y. Hence it may be integrated accurately using repeated Gauss–Legendre quadrature with weights w_i^{GL} and sample points $\xi_{\mathrm{GL}}^{(i)}$ on the normalized interval (0,1) that is used to approximate each integral of the double integral. The lower and upper limits of the inner integral in (10) are, from (9), $u_{L,U}\equiv u(x_{L,U})$, and $u_{L,U}^{(j)}$ are the corresponding jth sampled values along y'. The quantities $\mathbf{r}'^{(i,j)}$ and $R^{(i,j)}=\sqrt{(y'^{(j)})^2+z^2}\cosh u^{(i)}$ denote sampled values of the position vector and R, respectively, but are more simply evaluated if the sample points in (u,y) are mapped back to the original triangle coordinates as discussed below [see (18)].

We finally obtain (3) by summing similar contributions from all three subtriangles; it is convenient, however, to express the overall quadrature scheme in the form

$$\mathbf{I}\approx\mathcal{J}\sum_k W_k\boldsymbol{\Lambda}(\mathbf{r}'^{(k)})\frac{e^{-jkR^{(k)}}}{4\pi R^{(k)}} \tag{11}$$

where W_k are weights corresponding to area coordinate sample points [$\xi_1^{(k)}$, $\xi_2^{(k)}$, $\xi_3^{(k)}$] of the *original* triangle of area A and unit normal $\hat{\mathbf{n}}$. In this form, the homogeneous medium Green's function in (11) may be replaced by *any* Green's function with a $1/R$ singularity. Also, from a programming standpoint, we are then able to essentially hide apparent differences between integration over smooth versus non-smooth integrands (except that in the latter case, the weights and sample points depend on $\mathbf{r}_0$). In (11), $\mathcal{J}=2A$ is the Jacobian of the transformation between global and parametric coordinates on the triangle and, comparing (10) and (11), W_k is a concatenated listing of the now-dimensionless weights

$$W_k = (\hat{\mathbf{n}}\cdot\hat{\mathbf{n}}')\frac{w_iw_jh_1'\left(u_U^{(j)}-u_L^{(j)}\right)R^{(i,j)}}{\mathcal{J}} \tag{12}$$

arising from each subtriangle, with the double index (i,j) mapped to a single index k. The factor $\hat{\mathbf{n}}\cdot\hat{\mathbf{n}}'$, where $\hat{\mathbf{n}}'$ is the unit normal of the subtriangle, is included to extend the method to near-singularities that occur when the projected observation point falls outside the original triangle. In this case, at least one of the subtriangles lies entirely outside the source triangle. The factor $\hat{\mathbf{n}}\cdot\hat{\mathbf{n}}'$ makes its weights negative, and its contribution then cancels those from partial domains of subtriangles that extend outside the original triangle [see Fig. 4(b)].

Finally, to complete the mapping of quadrature data back to the original triangle, we map the sample points in the (u,y') domain back to area coordinates ($\xi_1^{(k)}$, $\xi_2^{(k)}$, $\xi_3^{(k)}$) of the original triangle as follows. First, the y' samples are given by

$$y'^{(j)} = h_1'\left(1-\xi_1'^{(i,j)}\right),\quad \xi_1'^{(i,j)}\equiv\xi_{\mathrm{GL}}^{(j)} \tag{13}$$

and then we use (6) and (7) to determine $x_{L,U}^{(j)}=x_{L,U}(y'^{(j)})$.

Next, we calculate $u_{L,U}^{(j)}\equiv u\left(x_{L,U}^{(j)}\right)$ from (9)—noting that if $z=0$, then $u_{L,U}^{(j)}$ are constant—and find the u samples from

$$u^{(i,j)} = u_L^{(j)}\left(1-\xi_{\mathrm{GL}}^{(i)}\right)+u_U^{(j)}\xi_{\mathrm{GL}}^{(i)}. \tag{14}$$

The corresponding x' samples are then found from (9)

$$x'^{(i,j)} = \sqrt{(y'^{(j)})^2+z^2}\sinh u^{(i,j)} \tag{15}$$

and, hence, the remaining subtriangle area coordinates are

$$\begin{aligned}\xi_3'^{(i,j)} &= \frac{\hat{\mathbf{n}}'\cdot\boldsymbol{\ell}_3'\times\left(\hat{\mathbf{h}}_1'y'^{(j)}-\hat{\boldsymbol{\ell}}_1x'^{(i,j)}\right)}{2A'} \\ \xi_2'^{(i,j)} &= 1-\xi_3'^{(i,j)}-\xi_1'^{(j)}.\end{aligned} \tag{16}$$

Finally, the mappings from subtriangle back to original triangle coordinates are given by

$$\begin{aligned}\begin{bmatrix}\xi_1^{(k)}\\ \xi_2^{(k)}\\ \xi_3^{(k)}\end{bmatrix} &= [T]\begin{bmatrix}\xi_1'^{(i,j)}\\ \xi_2'^{(i,j)}\\ \xi_3'^{(i,j)}\end{bmatrix} \\ [T] &= \begin{bmatrix}\xi_1^0 & 0 & 0\\ \xi_2^0 & 1 & 0\\ \xi_3^0 & 0 & 1\end{bmatrix}\rightarrow\begin{bmatrix}\xi_1^0 & 0 & 1\\ \xi_2^0 & 0 & 0\\ \xi_3^0 & 1 & 0\end{bmatrix}\rightarrow\begin{bmatrix}\xi_1^0 & 1 & 0\\ \xi_2^0 & 0 & 1\\ \xi_3^0 & 0 & 0\end{bmatrix}\end{aligned} \tag{17}$$

where (ξ_1^0, ξ_2^0, ξ_3^0) are the area coordinates of the projected observation point and the index correspondence $k\leftrightarrow(i,j)$ pairs sample points with their corresponding weights. Again, the arrows indicate permutations on the right-hand side of the equalities needed to go from treating subtriangle 1 to subtriangles 2 and 3 of Fig. 1. The sampled values of R in (12) are now simply

$$R^{(i,j)} = \left|\mathbf{r}-\mathbf{r}_1\xi_1^{(k)}-\mathbf{r}_2\xi_2^{(k)}-\mathbf{r}_3\xi_3^{(k)}\right|. \tag{18}$$

To extend the method to integration over rectangular domains, we simply split the domain into four rather than three

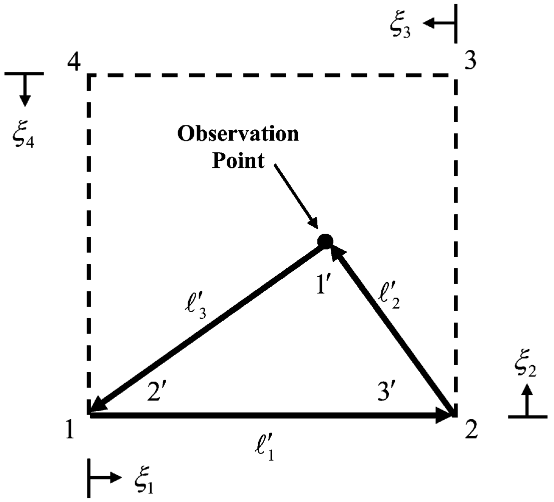

Fig. 3. Geometry of a parent quadrilateral and a subtriangle.

subtriangles and repeat the procedure above. The major difference is in the transformation from subtriangle coordinates back to rectangle coordinates. For example, consider the parallelogram in Fig. 3 with normalized coordinates satisfying $\xi_1+\xi_3=1$ and $\xi_2+\xi_4=1$. The relationship between the local and global coordinates for each of the subtriangles is given by

$$\begin{aligned}\mathbf{r}'_1 &= \mathbf{r}_0\\ \mathbf{r}'_2 &= \mathbf{r}_1 \rightarrow \mathbf{r}_2 \rightarrow \mathbf{r}_3 \rightarrow \mathbf{r}_4\\ \mathbf{r}'_3 &= \mathbf{r}_2 \rightarrow \mathbf{r}_3 \rightarrow \mathbf{r}_4 \rightarrow \mathbf{r}_1.\end{aligned} \tag{19}$$

The mappings from subtriangle to original triangle coordinates are given by

$$\begin{aligned}\begin{bmatrix}\xi_1^{(\ell,k)}\\ \xi_2^{(\ell,k)}\\ \xi_3^{(\ell,k)}\\ \xi_4^{(\ell,k)}\end{bmatrix} &= [T]\begin{bmatrix}\xi_1^{\prime(\ell,k)}\\ \xi_2^{\prime(\ell,k)}\\ \xi_3^{\prime(\ell,k)}\end{bmatrix}\\ [T] &= \begin{bmatrix}\xi_1^o & 0 & 1\\ \xi_2^o & 0 & 0\\ \xi_3^o & 1 & 0\\ \xi_4^o & 1 & 1\end{bmatrix} \rightarrow \begin{bmatrix}\xi_1^o & 1 & 1\\ \xi_2^o & 0 & 1\\ \xi_3^o & 0 & 0\\ \xi_4^o & 1 & 0\end{bmatrix}\\ &\rightarrow \begin{bmatrix}\xi_1^o & 1 & 0\\ \xi_2^o & 1 & 1\\ \xi_3^o & 0 & 1\\ \xi_4^o & 0 & 0\end{bmatrix} \rightarrow \begin{bmatrix}\xi_1^o & 0 & 0\\ \xi_2^o & 1 & 0\\ \xi_3^o & 1 & 1\\ \xi_4^o & 0 & 1\end{bmatrix}.\end{aligned} \tag{20}$$

B. *Results for a Triangular Element*

Before presenting numerical results, it is instructive to look at the distribution of sample points produced by the singularity cancellation method in order to graphically understand how near-singularities are handled. The geometry being used is that of [7], a right triangle with vertices at (0,0,0) (0.1λ, 0, 0), (0, 0.1λ, 0), and $\lambda = 10$ [m]. Fig. 4(a) and (b) shows the clustering of the sample points around a singular and near-singular observation point, respectively, in the plane of the triangle. Note that subtriangles 1 and 3 in Fig. 4(b) are partially outside the original triangle, but the excess potential integral contributions from their exterior domains are canceled by subtriangle 2's contribution since it overlaps them and has negative weights. As long as the method is used only when the projected observation point is near the triangle, the subtriangles always have quite different shapes and substantially differing potential contributions; hence there is negligible loss in accuracy due to cancellation effects. Also note that [see (10)] for a constant basis function, the static kernel $(k = 0)$ may be integrated *exactly* using only one sample point per subtriangle; indeed, this case reduces to the results in [4]. This feature helps to explain the method's efficiency relative to other approaches.

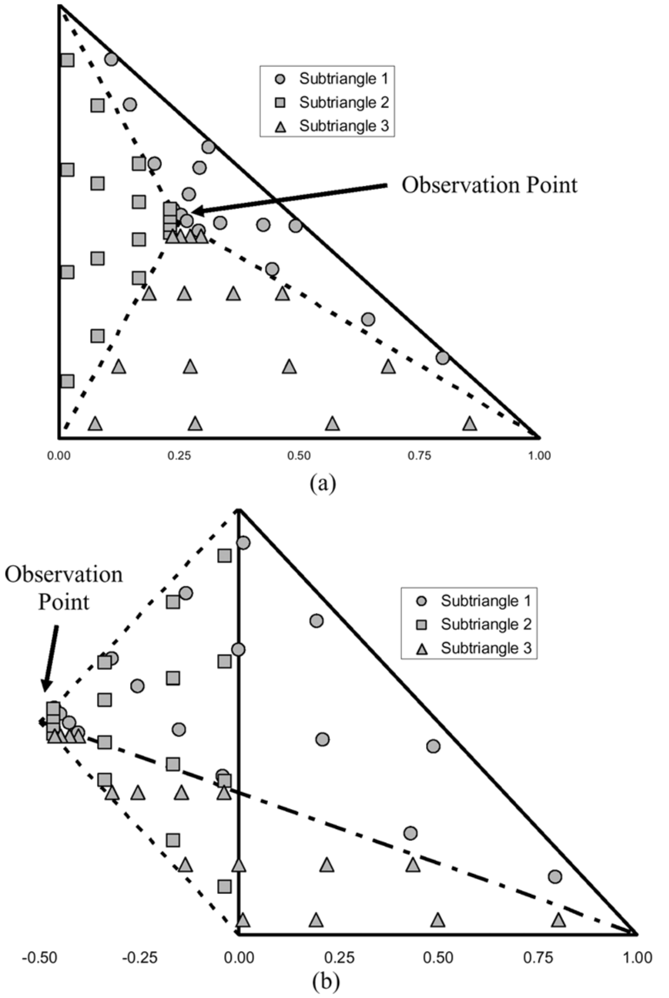

Fig. 4. Distribution of sample points for (a) singular observation point and (b) near-singular observation point.

Numerical results for four different observation points are presented inTable I for the right triangle of [7]. (Note that the subtriangles, however, are *not* right triangles.) As in [7], all four observation points lie in the plane of the triangle and the integrand used in the potential calculation is e^{-jkR}/R. The last row of the table shows the reference calculation of [7] using the software package *Mathematica*. Recall that the current method uses a product of two Gauss–Legendre sampling schemes—one in the transverse direction corresponding to sampling at a fixed value of y' and one in the radial direction corresponding to the fixed value of x'. For each observation point, the current

TABLE I
COMPARISON OF NUMERICAL RESULTS FOR INTEGRATING A SINGULARITY ON A TRIANGLE AT FOUR DIFFERENT OBSERVATION POINTS

Observation Point Location (x,y,z) [m]	**(0.1, 0.1,0.0)**	**(0.2, 0.2,0.0)**	**(0.3, 0.3,0.0)**	**(0.4, 0.4,0.0)**
Cancellation Scheme Total Sample Points = 12 Radial Samples = 2 Transverse Samples = 2	1.900764 – j 0.3072100	2.248722 – j 0.3083719	2.383519 – j 0.3084644	2.286197 – j 0.3073284
Rossi and Cullen Total Sample Points = 24	1.89818 – j 0.309025	2.24628 – j 0.31111	2.38100 – j 0.311817	2.28374 – j 0.311502
Cancellation Scheme Total Sample Points = 18 Radial Samples = 2 Transverse Samples = 3	1.898717 – j 0.3096465	2.246418 - j 0.3111560	2.381171 – j 0.3118219	2.284133 – j 0.3115903
Rossi and Cullen Total Sample Points = 30	1.89853 – j 0.309515	2.24629 – j 0.311141	2.381 – j 0.31187	2.28386- j 0.311661
Cancellation Scheme Total Sample Points = 24 Radial Samples = 2 Transverse Samples = 4	1.898567 – j 0.3096465	2.246282 - j0.3111464	2.381004 - j0.3118307	2.283886 - j0.3116952
Cancellation Scheme Total Sample Points = 36 Radial Samples = 3 Transverse Samples = 4	1.898579 – j 0.3096492	2.246288 – j 0.3111477	2.381009 – j 0.3118314	2.283890 – j 0.3116960
Rossi and Cullen Mathematica	**1.89857 – j 0.309643**	**2.24628 – j 0.311144**	**2.38099 – j 0.311826**	**2.28386 – j 0.311688**

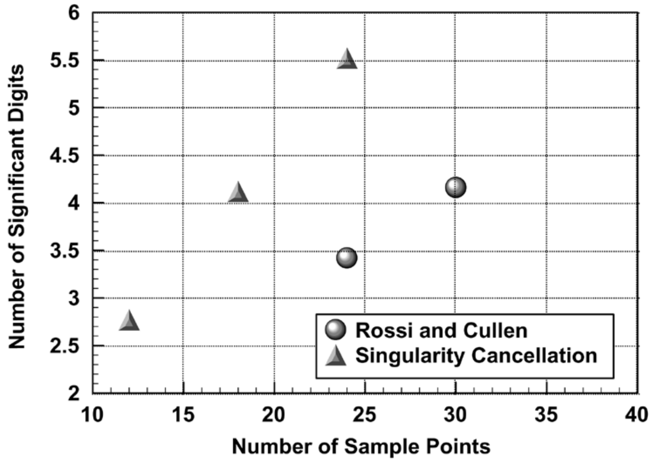

Fig. 5. Singular integration convergence comparison.

method converges toward the reference result. To see the convergence more clearly, Fig. 5 shows the number of significant figures that agree with the reference result at the observation point $(x, y, z) = (0.01\lambda, 0.01\lambda, 0)$ versus the number of sample points.

The reference result provided in [7] has only six significant figures. Hence, to see the convergence trend to a higher order of accuracy, a reference potential was calculated at the four observation points to 14 significant figures using the singularity cancellation method. These values were validated by analyzing a large number of cases involving different combinations of radial and transverse Gauss–Legendre sampling schemes. The final results appearing in Table II represent combinations that minimize the number of samples for convergence to the number of significant digits of the table. It is likely that further minimization of the number of samples could still be achieved since, for simplicity, the same sampling scheme was used in each of the subtriangles. The rate of convergence was found to be essentially independent of observation point and the result for $(x, y, z) = (0.01\lambda, 0.01\lambda, 0)$ shown in Fig. 6 is typical. The reader should keep in mind, however, that efficiency is not our principal motivation; our interest is more in a simple, arbitrarily accurate, and robust scheme that fits well into the object-oriented approach. Fig. 7 shows the real part of the potential for $(y, z) = (0.5, 0.0)$ as a function of x. This figure merely verifies that the potential is continuous but has an infinite slope as the observation point moves across the triangle's boundaries.

No calculations were performed in [7] for near-singularities where the observation point lies outside the plane of the source triangle. A convergence study was therefore performed using the singularity cancellation method for the same geometry as before, but with the observation points located at $(x, y, z) = (0.1, 0.1, d)$ [m], where $d = 0.0001, 0.01,$ and 0.1 [m].

In analyzing near-singularities, it was found that, in order to achieve sufficient accuracy, the subtriangles had to be subdivided along the radial direction, especially when d was extremely small but nonvanishing. The reason for this lies in understanding the mapping of the domain where the integral is being calculated. Recall that, after transforming into the u domain, the upper limit in (10) is given by

$$u_U(x') = \sinh^{-1} \frac{x'}{\sqrt{(y')^2 + z^2}}. \tag{21}$$

From Fig. 2, we can define $\tan(\phi_U) = y'/x'_U$, which yields

$$u_U(x') = \sinh^{-1} \frac{\frac{y'}{\tan(\phi_U)}}{\sqrt{(y')^2 + z^2}}. \tag{22}$$

Fig. 8 plots u_U versus y' for $\tan(\phi_U) = 1$ and $z = 0.0001, 0.01,$ and 0.1 [m]. The lower integration limit would yield a similar plot and the domain of integration lies

TABLE II
REFERENCE POTENTIAL VALUES

Radial	Transverse	Total	x [m]	y [m]	Real (Potential)	Imaginary (Potential)
9	16	432	0.1	0.1	1.89857266176845	-0.30964308563686
5	32	480	0.2	0.2	2.24628500696514	-0.31114351821225
6	12	216	0.3	0.3	2.38100297872747	-0.31182631634521
5	32	480	0.4	0.4	2.28386985510842	-0.31168824333213

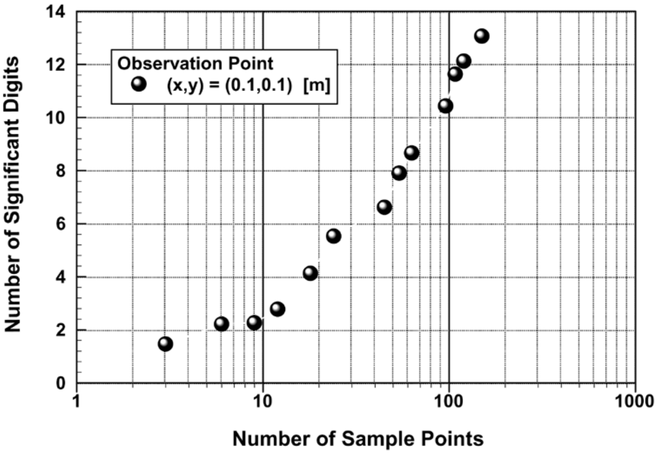

Fig. 6. Convergence of singularity cancellation scheme for a self-term.

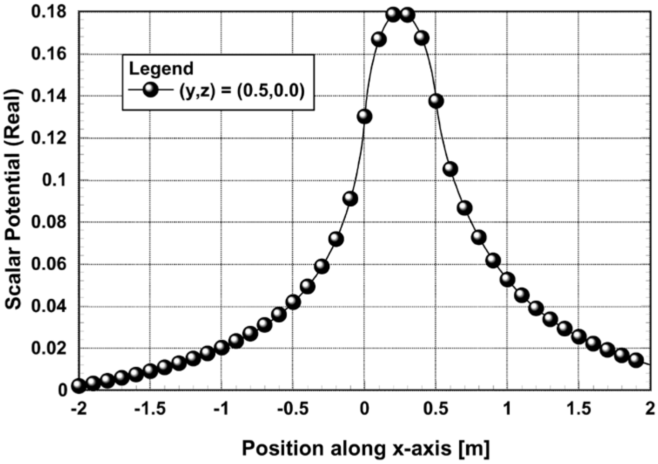

Fig. 7. The real part of the potential.

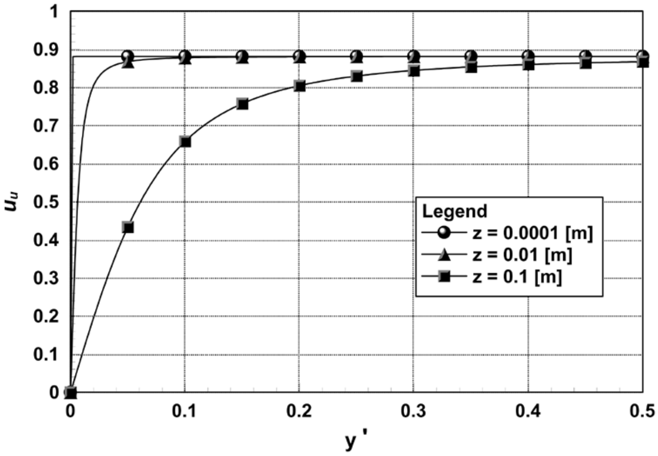

Fig. 8. Mapped domain of integration as the observation point moves off the surface.

between the two curves. From the expressions above, we see that, for $z = 0$, the triangular domain is mapped into a rectangle because u_U and u_L are constant. As the observation point moves off the surface, however, $u_{L,U} \to 0$ as $y' \to 0$. This rapid change in the domain limits the accuracy of the integration. Note that if the near-singularity lies in the plane of the triangle $(d = 0)$, this problem does not occur.

To overcome this difficulty, we chose to split the subtriangles along the radial direction at $y' = 0.5d$ and $y' = 3.0d$ and to use a Gauss–Legendre scheme in each of the resulting three regions. For simplicity, the same Gauss–Legendre scheme was used in each region of the subtriangle, and for all three subtriangles. Clearly one could further optimize the choice of splitting points and sample point distributions within the split subtriangles to minimize the number of sample points. Table III shows the reference value for the three different observation points to 14 significant digits for $(x, y, z) = (0.1, 0.1, d)$ [m], where $d = 0.0001, 0.01$, and 0.1 [m]. The radial and transverse sampling schemes of the table represent the combinations that minimize the number of samples for a given accuracy. A plot of the convergence relative to the reference values in Table III is shown in Fig. 9. Note that, as we move further off the surface, $u_{L,U}$ in Fig. 8 becomes much smoother and, therefore, increasing the number of sample points by a modest amount increases the accuracy.

For the triangle under consideration, we have seen that to achieve a desired accuracy the number of sample points must be increased as the observation point moves out of the source plane. It is important to note, however, that the more difficult cases examined above represent extremely small distances relative to triangle size that often do not occur in applications. As Fig. 9 shows, for even very small distances, the method easily produces the three to four significant digit accuracy that is usually needed. This is in contrast to the Duffy method, for instance, and it is in this sense that the method may be considered a comprehensive approach for treating both singular and near-singular integrals.

The results shown up to this point have been obtained assuming a constant source density or basis function. Of interest, however, is the convergence of the scheme for higher order bases. Therefore, as a final example for 2-D geometries, we plot the convergence relative to the reference values generated in Table IV for a quartic (scalar) source density. Three observation points were considered for the right triangle used in the previous examples. The results are shown in Fig. 10, where the quartic source density is ξ_1^4. As expected, the convergence rates are similar to those of Figs. 6 and 9, but a few more sample points are needed to obtain a given accuracy level.

TABLE III
REFERENCE VALUES FOR NEAR-SINGULARITIES

Radial	Transverse	Total	x [m]	y [m]	z [m]	Real	Imaginary
32	12	3456	0.1	0.1	0.0001	1.89795445129807	-0.30964308543194
32	24	6912	0.1	0.1	0.01	1.83755816482970	-0.30964103642031
32	24	6912	0.1	0.1	0.1	1.42970516324653	-0.30943820412320

TABLE IV
REFERENCE VALUES FOR SINGULARITIES USING QUARTIC BASIS FUNCTIONS

Radial	Transverse	Total	x [m]	y [m]	z [m]	Real	Imaginary
6	20	360	0.1	0.1	0.0	0.37918591657965	-0.02089680301877
32	24	6912	0.1	0.1	0.0001	0.37893270526228	-0.02089680300501
32	16	4608	0.1	0.1	0.01	0.35433936106655	-0.02089666539961

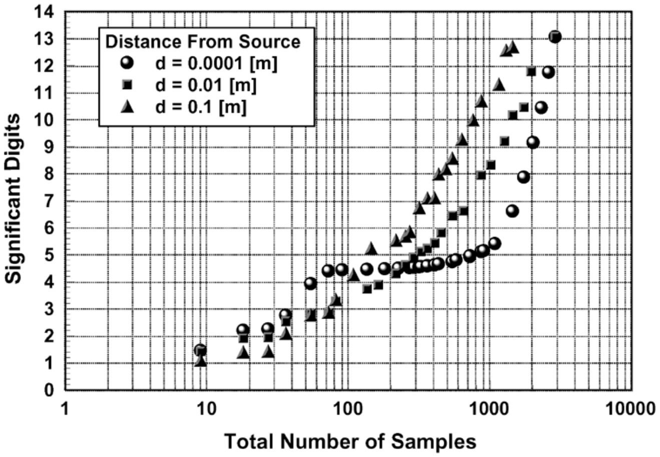

Fig. 9. Convergence for near-singularities.

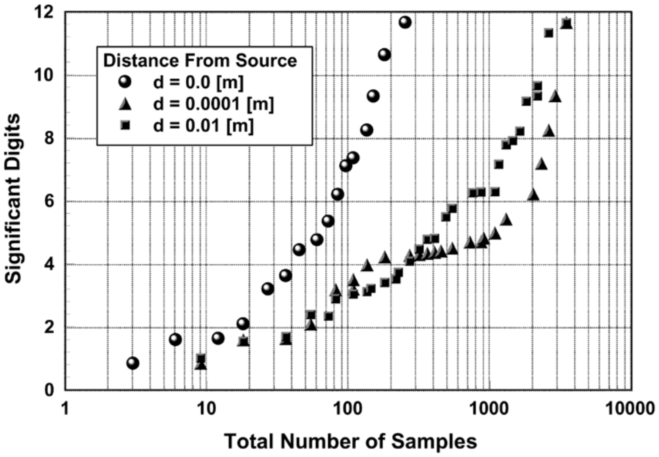

Fig. 10. Convergence using quartic basis functions.

The number of sample points needed for a given accuracy is expected to increase if 1) higher order bases are used, 2) the electrical size of the triangle increases, or 3) the triangle is curved. We do not examine these cases here, but remark that the latter case is handled by using the weights and sample points obtained by applying the present scheme on the planar triangle tangent to the original triangle at the projected observation point and having the same position vector derivatives with respect to area coordinates as the original (curved) triangle there [11].

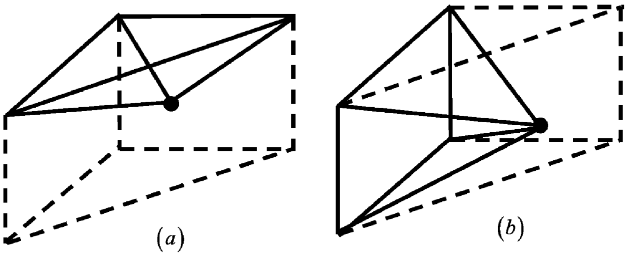

Fig. 11. Subdividing a prism about the observation point. (a) A subtetrahedron and (b) a subpyramid.

III. 3-D GEOMETRY—TETRAHEDRONS, BRICKS, AND PRISMS

The previous analysis is easily extended to three common volume elements: tetrahedrons, bricks and prisms. Recall that by subdividing the 2-D geometry about the observation point we achieved the property that the method exactly integrates a singular kernel having the static form $1/R$. To retain a similar property in the 3-D case, we must again subdivide the geometry about the observation point. The procedure is illustrated in Fig. 11(a) and (b) for a prism, where we show a subtetrahedron and a subpyramid, respectively. We illustrate the procedure with a prism because it has both triangular and rectangular faces, leading to subelements that are tetrahedrons and pyramids, respectively. Indeed, all the 3-D geometries we analyze can be similarly subdivided into subtetrahedrons and/or subpyramids.

In order to make use of the previous 2-D analysis, we further subdivide the subtetrahedrons and subpyramids into layers of triangles and quadrilaterals, respectively. For example, Fig. 12 shows a subtetrahedron with a stack of three triangles representing three sample points along the height of the subtetrahedron. Note that the height of the subtetrahedron is defined from the observation point to the face of the prism and the triangles are stacked perpendicular to this height. The ratio of a triangle's distance from the observation point to one of its edges remains fixed, and hence the problem of small z relative to an edge only occurs for degenerate subtetrahedrons (observation point near a face of the original tetrahedron). Thus, integrating a 3-D element reduces to integrating a stack of 2-D elements, each of whose cross-section integrals are relatively simple. Furthermore, since the 2-D integration handles the near-singularity, we can use a simple Gauss–Legendre scheme for sampling in the third dimension. We summarize the procedure as follows.

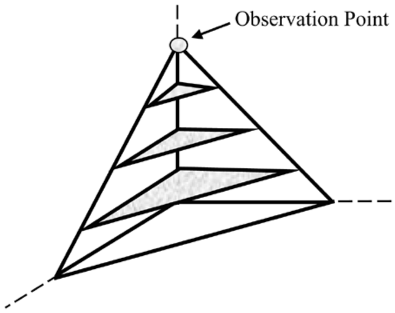

Fig. 12. Subtetrahedron with three layers of triangles.

1) Subdivide the element about the observation point into subvolume elements.
2) For each subelement, choose the number of Gaussian sample points along the height. The subelement cross-section at each sample point is a 2-D element.
3) Find the vertices of the 2-D subelement (triangle or quadrilateral) and the position of the observation point with respect to the 2-D subelement.
4) Calculate sample points and weights for the 2-D subelement using the scheme detailed in the previous section.
5) Map the local subelement sample points back to the global coordinate system.

A. Weights and Sample Points for a Prism

Consider the geometries of a subtetrahedron and subpyramid shown in Fig. 13(a) and (b), respectively. Geometrical parameters for the subelements are denoted by primes. When integrating a volume element, it is important to use a consistent notation for labeling the vertices. For example, in Fig. 13(a), the global vertices are labeled such that if the fingers of the right hand curl around vertices 1, 2, and 3, then the thumb points into the volume element. Similarly for the subelement, if the fingers curl around the vertices $1'$, $2'$, and $4'$, then the thumb points into the volume element. For this paper, the observation point is labeled $3'$ for a subtetrahedron and $5'$ for a subpyramid.

The integration over a subtetrahedron is given by

$$\mathbf{I} = \int_0^{h_v} \int_0^{h} \int_{x_L}^{x_U} \mathbf{\Lambda}(x', y', z') \frac{e^{-jkR}}{4\pi R} dx' dy' dz'. \tag{23}$$

Note that the subscript v in the limit of the integral is used to indicate integration along the height of the volume subelement, which distinguishes it from the height h used for triangles. The two inner integrals represent the potential from a triangular source distribution at the cross-section for a nearby (near-singular) observation point. The result is given by

$$\int_0^{h} \int_{x_L}^{x_U} \mathbf{\Lambda}(x', y', z') \frac{e^{-jkR}}{4\pi R} dx' dy' \approx 2A^e(z') \sum_{k=1}^{K} \sum_{j=1}^{J} W_{jk} \mathbf{\Lambda}(x'^{(j,k)}, y'^{(k)}, z') \frac{e^{-jkR^{(j,k)}}}{4\pi R^{(j,k)}} \tag{24}$$

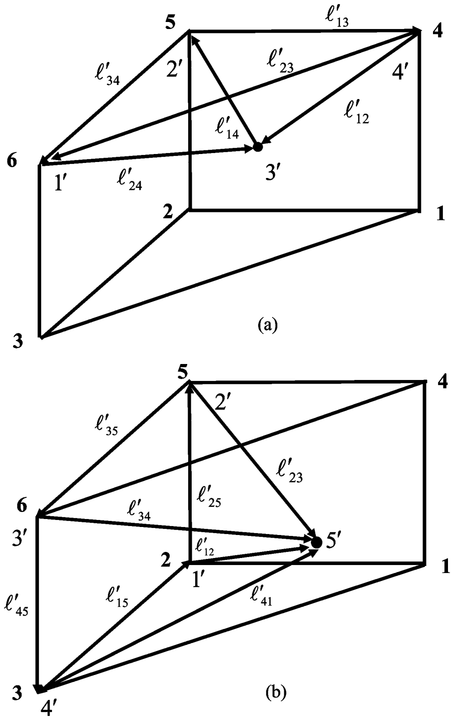

Fig. 13. (a) Subtetrahedron and (b) subpyramid geometries for a prism.

where W_{jk} are the weights given by (12) and $2A^e(z')$ is the Jacobian of the triangle at the cross-section location. Substituting (24) into (23) yields

$$\mathbf{I} \approx \int_0^{h_v} 2A^e(z') \sum_{k=1}^{K} \sum_{j=1}^{J} W_{jk} \mathbf{\Lambda}(x'^{(j,k)}, y'^{(k)}, z') \times \frac{e^{-jkR^{(j,k)}}}{4\pi R^{(j,k)}} dz'. \tag{25}$$

Normalizing the remaining integration interval and applying a Gaussian scheme yields

$$\mathbf{I} \approx 2h_v \sum_{\ell=1}^{L} A_\ell^e \sum_{k=1}^{K} \sum_{j=1}^{J} w_\ell W_{jk\ell} \mathbf{\Lambda}(x'^{(j,k,l)}, y'^{(k)}, z'^{(\ell)}) \times \frac{e^{-jkR^{(j,k,\ell)}}}{4\pi R^{(j,k,\ell)}}. \tag{26}$$

We note that the changing area A_ℓ^e of the triangular cross-section at the $\boldsymbol{\ell}$th sample point is given by

$$A_\ell^e = \left(1 - \xi_{\mathrm{GL}}'^{(\ell)}\right)^2 A^b \tag{27}$$

where A^b is the area of the base of the subtetrahedron and $\xi_{\mathrm{GL}}'^{(\ell)}$ is the normalized Gauss–Legendre coordinate that vanishes on A^b and is unity at the observation point. Equation (26) now becomes

$$\mathbf{I} \approx 2h_v A^b \sum_{j=1}^{J} \sum_{k=1}^{K} \sum_{\ell=1}^{L} \left(1 - \xi_{\mathrm{GL}}'^{(\ell)}\right)^2 w_\ell W_{jk} \times \mathbf{\Lambda}(x'^{(j,k,\ell)}, y'^{(k)}, z'^{(\ell)}) \frac{e^{-jkR^{(j,k,\ell)}}}{4\pi R^{(j,k,\ell)}} \tag{28}$$

where $\mathcal{J}_{\text{subtet}} = 2h_v A^b$ is the Jacobian of the subtetrahedron. The weights for the subtetrahedron are therefore given by

$$W_{jk\ell} = \sigma_m \frac{\mathcal{J}_{\text{subtet}} \left(1 - \xi_{\text{GL}}^{\prime(\ell)}\right)^2 w_\ell W_{jk}}{\mathcal{J}_{\text{prism}}} \tag{29}$$

where $\mathcal{J}_{\text{prism}}$ is the Jacobian associated with the global prism element.

In order to handle near-singularities, we introduce the factor $\sigma_m = \pm 1$ given by

$$\sigma_m = \frac{\boldsymbol{\ell}'_{24} \cdot (\boldsymbol{\ell}'_{13} \times \boldsymbol{\ell}'_{34})}{\left|\boldsymbol{\ell}'_{24} \cdot (\boldsymbol{\ell}'_{13} \times \boldsymbol{\ell}'_{34})\right|} \tag{30}$$

for a subtetrahedron and

$$\sigma_m = \frac{\boldsymbol{\ell}'_{12} \cdot (\boldsymbol{\ell}'_{15} \times \boldsymbol{\ell}'_{25})}{\left|\boldsymbol{\ell}'_{12} \cdot (\boldsymbol{\ell}'_{15} \times \boldsymbol{\ell}'_{25})\right|} \tag{31}$$

for a subpyramid, with the subscript ^{m} denotes the subelement being analyzed. If the observation point is outside the global tetrahedron, then the weights for subtetrahedrons that lie completely outside the global element are negative.

The derivation of the weights for subpyramids follows that for subtetrahedrons with two exceptions: 1) the Jacobian of the quadrilateral in (25) is $A^e(z)$ instead of $2A^e(z)$ and 2) the Jacobian of the subpyramid is given by $\mathcal{J}_{\text{subpyr}} = 3V_{\text{subpyr}} = h_v A^b$. The weights for the subpyramids are thus given by

$$W_{jk\ell} = \sigma_m \frac{\mathcal{J}_{\text{subpyr}} \left(1 - \xi_{\text{GL}}^{\prime(\ell)}\right)^2 w_\ell W_{jk}}{\mathcal{J}_{\text{prism}}}. \tag{32}$$

We next consider the mapping of local coordinates back to the coordinates of the original prism. We illustrate this mapping first for the subtetrahedron and then for the subpyramid. In order to distinguish them from the global coordinates, the subvolume coordinates are primed while the 2-D layer coordinates are double-primed.

Consider the subtetrahedron in Fig. 13(a). We first find the vertices for the layers of triangles. Their position vectors are given by

$$\mathbf{r}''_1 = \mathbf{r}'_1 + \xi_{\text{GL}}^{\prime(\ell)} \boldsymbol{\ell}'_{24} \tag{33}$$

$$\mathbf{r}''_2 = \mathbf{r}'_2 - \xi_{\text{GL}}^{\prime(\ell)} \boldsymbol{\ell}'_{14} \tag{34}$$

and

$$\mathbf{r}''_3 = \mathbf{r}' + \xi_{\text{GL}}^{\prime(\ell)} \boldsymbol{\ell}'_{12} \tag{35}$$

where $\xi_{\text{GL}}^{\prime(\ell)}$ is the Gauss–Legendre sample point along the height of the subtetrahedron. Once the vertices of the triangle and the position of the observation point are known, we can use the 2-D scheme previously discussed to find the weights W_{jk} and sample points ($\xi_1^{\prime\prime(j,k)}$, $\xi_2^{\prime\prime(j,k)}$, $\xi_3^{\prime\prime(j,k)}$) on the triangle. The global position vector for the prism is then given by

$$\mathbf{r}_{\text{prism}} = \left(\mathbf{r}_6 + \xi_{\text{GL}}^{\prime(\ell)} \boldsymbol{\ell}'_{24}\right) \xi''_1 + \left(\mathbf{r}_5 - \xi_{\text{GL}}^{\prime(\ell)} \boldsymbol{\ell}'_{14}\right) \xi''_2 + \left(\mathbf{r}_4 + \xi_{\text{GL}}^{\prime(\ell)} \boldsymbol{\ell}'_{12}\right) \xi''_3. \tag{36}$$

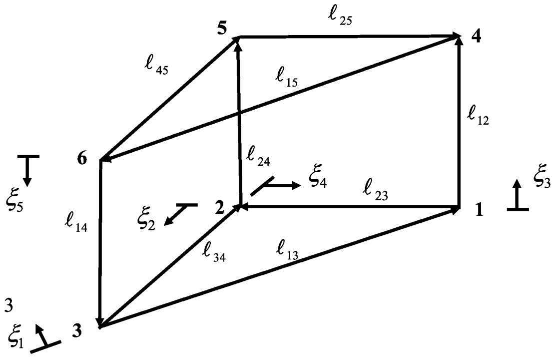

Fig. 14. Geometry of global prism.

TABLE V
GEOMETRY OF PRISM

Vertex	(x,y,z) [m]
1	(0,1,0)
2	(0,0,0)
3	(1,0,0)
4	(0,1,1)
5	(0,0,1)
6	(1,0,1)

In terms of normalized coordinates we have, from Fig. 14

$$\xi_1 = \frac{(\mathbf{r}_{\text{prism}} - \mathbf{r}_1) \cdot (\boldsymbol{\ell}_{15} \times \boldsymbol{\ell}_{12})}{\mathcal{J}} \tag{37}$$

$$\xi_2 = \frac{(\mathbf{r}_{\text{prism}} - \mathbf{r}_1) \cdot (\boldsymbol{\ell}_{12} \times \boldsymbol{\ell}_{23})}{\mathcal{J}} \tag{38}$$

$$\xi_3 = \frac{(\mathbf{r}_{\text{prism}} - \mathbf{r}_1) \cdot (\boldsymbol{\ell}_{13} \times \boldsymbol{\ell}_{34})}{\mathcal{J}} \tag{39}$$

$$\xi_4 = 1 - \xi_1 - \xi_2 \tag{40}$$

and

$$\xi_5 = 1 - \xi_3. \tag{41}$$

The sample points for the subpyramid are derived in the same manner, but the underlying 2-D subelements are now quadrilaterals. Based on the geometry in Fig. 13(b), the vertex position vectors of the quadrilateral are given by

$$\mathbf{r}''_1 = \mathbf{r}'_1 + \xi_{\text{GL}}^{\prime(\ell)} \boldsymbol{\ell}'_{12} \tag{42}$$

$$\mathbf{r}''_2 = \mathbf{r}'_2 + \xi_{\text{GL}}^{\prime(\ell)} \boldsymbol{\ell}'_{23} \tag{43}$$

$$\mathbf{r}''_3 = \mathbf{r}'_3 + \xi_{\text{GL}}^{\prime(\ell)} \boldsymbol{\ell}'_{34} \tag{44}$$

and

$$\mathbf{r}''_4 = \mathbf{r}'_4 + \xi_{\text{GL}}^{\prime(\ell)} \boldsymbol{\ell}'_{41}. \tag{45}$$

From the 2-D scheme, we obtain the weights W_{jk} and sample points ($\xi_1^{\prime\prime(j,k)}$, $\xi_2^{\prime\prime(j,k)}$, $\xi_3^{\prime\prime(j,k)}$, $\xi_4^{\prime\prime(j,k)}$) on the triangle. Using the geometry of the normalized coordinates as defined for the quadrilateral in Fig. 3, the global position vector for the prism is given by

$$\mathbf{r}_{\text{prism}} = \left(\mathbf{r}_2 + \xi_{\text{GL}}^{\prime(\ell)} \boldsymbol{\ell}'_{12}\right) \xi''_3 \xi''_4 + \left(\mathbf{r}_5 + \xi_{\text{GL}}^{\prime(\ell)} \boldsymbol{\ell}'_{23}\right) \xi''_4 \xi''_1 + \left(\mathbf{r}_6 + \xi_{\text{GL}}^{\prime(\ell)} \boldsymbol{\ell}'_{34}\right) \xi''_1 \xi''_2 + \left(\mathbf{r}_3 + \xi_{\text{GL}}^{\prime(\ell)} \boldsymbol{\ell}'_{41}\right) \xi''_2 \xi''_3.$$

The normalized coordinates are then given by (37)–(41).

TABLE VI
STATIC POTENTIAL FOR AN OBSERVATION POINT AT $(x, y, z) = (50, 50, 50)$

NUMBER OF SAMPLES ALONG HEIGHT	NUMBER OF SAMPLES ALONG THE RADIAL DIRECTION OF TRIANGLE	NUMBER OF SAMPLES ALONG THE TRANSVERSE DIRECTION OF TRIANGLE	TOTAL NUMBER OF SAMPLE POINTS IN PRISM	POTENTIAL WITH OUR SCHEME	POTENTIAL WITH GAUSSIAN SCHEME
1	6	1	108	4.63010811E-04	
1	8	1	144	4.63039839E-04	
1	10	1	180	4.63039849E-04	
			9		4.63039846E-04
			35		4.63039848E-04

TABLE VII
REFERENCE VALUES FOR THE POTENTIAL OF A PRISM

Vertical	Radial	Transverse	Total	x	y	z	Real	Imaginary
5	16	9	12960	0.333	0.333	0.5	0.1101990007812	-0.0246818749055
5	20	16	28800	0.333	0.333	1	0.07701456144055	-0.02427846658870
5	24	16	34560	0.333	0.333	1.25	0.04833922443213	-0.02377978649190

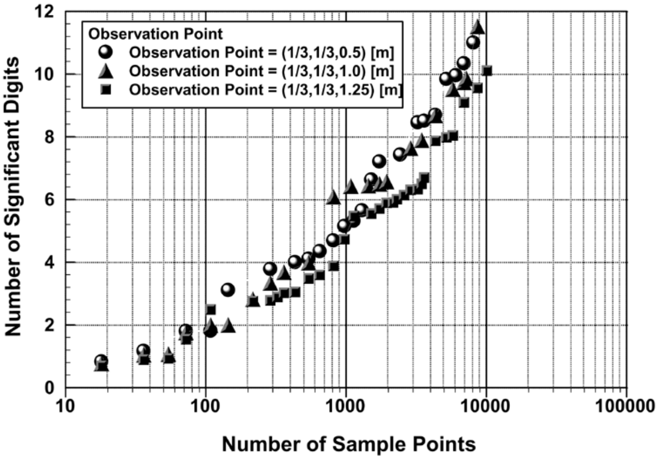

Fig. 15. Convergence of the potential for a prism.

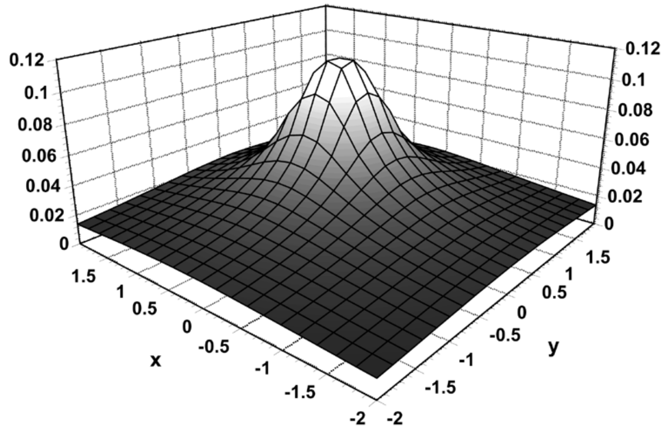

Fig. 16. The absolute value of the potential for a prism.

B. Numerical Results for a Prism

As a first check, we calculate the static potential in the far field of a prism with unit source density at an observation point $(x, y, z) = (50, 50, 50)$ [m]. At this location, the potential may be calculated using either the singularity cancellation method or a regular Gauss-tetrahedron integration scheme. The vertices of the prism are given in Table V. Results using the singularity cancellation scheme and regular Gauss-tetrahedron points are shown in Table VI. We see good agreement between the two methods. Note in particular that, as previously stated for the statics case, by dividing the prism about the observation point we only need one 2-D layer for each subvolume element in order to achieve convergence.

A convergence study was performed using the same geometry as above and a wavelength of 10 [m]. The observation points were located at $(x, y, z) = (1/3, 1/3, d)$, where $d = 0.5, 1.0,$ and 1.25 [m]. The convergence results are shown in Fig. 15, where the reference values are given in Table VII. Finally, in Fig. 16, we plot the absolute value of the potential for $z = 0.5$ [m] to check continuity as we move across the prism boundaries.

IV. CONCLUSION

A new integration scheme is presented that accurately and efficiently handles both singular and near-singular potential integrals with kernels of the form $1/R$. An important feature of the scheme is that it exactly integrates the free-space static potential of a constant source distribution on a triangle using only three sample points. Because the method also works for near-singular terms, potential integrals on triangular elements can be used as building blocks for evaluating potentials defined on other common elements. Detailed analyses and numerical results are presented for triangular and prism elements; the method is easily extended to quadrilaterals, bricks, and tetrahedrons.

Extensions of the method to treat the kernels of wire and body of revolution kernels have also been made. Furthermore, integrals involving kernels of the form $\text{grad}\ 1/R$ are also of interest and are currently under investigation. It is expected that results of these studies will be reported in the near future.

REFERENCES

[1] C. M. Butler, "Evaluation of potential integral at singularity of exact kernel in thin-wire calculations," *IEEE Trans. Antennas Propag.*, vol. AP-23, pp. 293–295, Mar. 1975.

[2] L. W. Pearson, "A separation of the logarithmic singularity in the exact kernel of the cylindrical antenna integral equation," *IEEE Trans. Antennas Propag.*, vol. AP-23, pp. 256–258, Mar. 1975.

[3] D. H. Werner, J. A. Huffman, and P. L. Werner, "Techniques for evaluating the uniform current vector potential at the isolated singularity of the cylindrical wire kernel," *IEEE Trans. Antennas Propag.*, vol. 42, pp. 1549–1553, Nov. 1994.

[4] D. R. Wilton, S. M. Rao, A. W. Glisson, D. H. Schaubert, O. M. Al-Bundak, and C. M. Butler, "Potential integrals for uniform and linear source distributions on polygonal and polyhedral domains," *IEEE Trans. Antennas Propag.*, vol. AP-32, pp. 276–281, Mar. 1984.

[5] R. D. Graglia, "On the numerical integration of the linear shape functions times the 3-D Green's function or its gradient on a plane triangle," *IEEE Trans. Antennas Propag.*, vol. 41, pp. 1448–1455, Oct. 1993.

[6] L. Knockaert, "A general Gauss theorem for evaluating singular integrals over polyhedral domains," *Electromagnetics*, vol. 11, pp. 269–280, 1991.

[7] L. Rossi and P. J. Cullen, "On the fully numerical evaluation of the linear-shape function times the 3-D Green's function on a plane triangle," *IEEE Trans. Microwave Theory Tech.*, vol. 47, pp. 398–402, Apr. 1999.

[8] T. F. Eibert and V. Hansen, "On the calculation of potential integrals for linear source distributions on triangular domains," *IEEE Trans. Antennas Propag.*, vol. 43, pp. 1499–1502, Dec. 1995.

[9] B. M. Notaros and B. D. Popovic, "Optimized entire-domain moment-method analysis of 3D dielectric scatterers," *Int. J. Numer. Model.*, vol. 10, pp. 177–192, 1997.

[10] S. Järvenpää, M. Taskinen, and P. Ylä-Oijala, "Singularity extraction technique for integral equation methods with higher order basis functions on plane triangles and tetrahedra," *Int. J. Numer. Meth. Eng.*, vol. 58, pp. 1149–1165, Aug. 2003.

[11] W. J. Brown and D. R. Wilton, "Singular basis functions and curvilinear triangles in the solution of the electric field integral equation," *IEEE Trans. Antennas Propag.*, vol. 47, pp. 347–353, Feb. 1999.

[12] W. A. Johnson, R. E. Jorgenson, L. K. Warne, J. D. Kotulski, J. B. Grant, R. M. Sharpe, N. J. Champagne, D. R. Wilton, and D. R. Jackson, "Our experiences with object oriented design, Fortran 90, and massively parallel computations," in *USNC/URSI Nat. Radio Science Meeting Dig.*, Atlanta, GA, Jun. 1998, pp. 308–308.

[13] M. G. Duffy, "Quadrature over a pyramid or cube of integrands with a singularity at a vertex," *SIAM J. Numer. Anal.*, vol. 19, no. 6, pp. 1260–1262, 1982.

[14] A. H. Stroud, *Approximate Calculation of Multiple Integrals*. Englewood Cliffs, NJ: Prentice-Hall, 1971, pp. 31–32.

[15] R. D. Graglia, "Static and dynamic potential integrals for linearly varying source distributions in two- and three-dimensional problems," *IEEE Trans. Antennas Propag.*, vol. AP-35, pp. 662–669, Jun. 1987.

[16] S. Caorsi, D. Moreno, and F. Sidoti, "Theoretical and numerical treatment of surface integrals involving the free-space Green's function," *IEEE Trans. Antennas Propag.*, vol. 41, pp. 1296–1301, Sep. 1993.

[17] D. Rosen and D. E. Cormack, "The continuation approach: A general framework for the analysis and evaluation of singular and near-singular integrals," *SIAM J. Appl. Math.*, vol. 55, no. 3, pp. 723–762, 1995.

[18] J. T. Beale and M. Lai, "A method for computing nearly singular integrals," *SIAM J. Numer. Anal.*, vol. 38, no. 6, pp. 1902–1925, 2001.

[19] J. M. Jin, *The Finite Element Method in Electromagnetics*, 2nd ed. New York: Wiley, 2002.

Michael A. Khayat (S'99–M'04) was born in Houston, TX, in 1972. He received the B.S., M.S., and Ph.D. degrees in electrical engineering from the University of Houston, in 1996, 1999, and 2003, respectively.

In December 2003, he joined the Antenna Group in the Avionic Systems Division at NASA Johnson Space Center. His current interests include antenna theory and design and computational electromagnetics.

Donald R. Wilton (S'63–M'65–SM'80–F'87) was born in Lawton, OK, October 25, 1942. He received the B.S., M.S., and Ph.D. degrees from the University of Illinois, Urbana-Champaign, in 1964, 1966, and 1970, respectively.

From 1965 to 1968, he was with Hughes Aircraft Co., Fullerton, CA, engaged in the analysis and design of phased array antennas. From 1970 to 1983, he was with the Department of Electrical Engineering, University of Mississippi. Since 1983, he has been a Professor of electrical engineering at the University of Houston, Houston, TX. From 1978 to 1979, he was a Visiting Professor at Syracuse University. During 2004–2005, he was a Visiting Scholar at the Polytechnic of Turin, Italy, the Sandia National Laboratories, and the University of Washington. His primary research interest is in computational electromagnetics, and he has published, lectured, and consulted extensively in this area.

Dr. Wilton has served the IEEE Antennas and Propagation Society as an Associate Editor of the IEEE TRANSACTIONS ON ANTENNAS AND PROPAGATION, as a Distinguished National Lecturer, and as a member of the AdCom. He received the IEEE Third Millenium Medal. He is a member of Commission B of URSI, in which he has held various offices, including Chair of U.S. Commission B.